Acta Crystallographica Section B
Structural Science
ISSN 0108-7681

Phase transition at high pressure in $Cu_2CO_3(OH)_2$ related to the reduction of the Jahn–Teller effect

Marco Merlini,[a]* Natale Perchiazzi,[b] Michael Hanfland[c] and Alexei Bossak[c]

[a]Dipartimento di Scienze della Terra, Università degli Studi di Milano, Via Botticelli, 23, Milano 20133, Italy, [b]Dipartimento di Scienze della Terra, Università di Pisa, via S. Maria 53, Pisa 56126, Italy, and [c]ESRF, European Synchrotron Radiation Facility, Grenoble, France

Correspondence e-mail: marco.merlini@unimi.it

Received 12 March 2012
Accepted 14 March 2012

Hydroxycarbonates with the general formula $Me_2(CO_3)(OH)_2$ are widely used materials in industrial processes and are widespread in nature. The Cu term, malachite, $Cu_2CO_3(OH)_2$, is monoclinic, $P2_1/a$. Substitution of Cu^{2+} with other bivalent cations such as Mg, Zn, Fe, Cu or Ni is possible and leads to a different structure type, rosasite, $P2_1/a$ or $P2_1/b11$ in the same cell setting as malachite. Rosasite structure is topologically similar to malachite, but the symmetry elements are oriented differently with respect to structural units. The stability of the malachite-like structure (MS) compared with the rosasite-like structure (RS) has been suggested to be related to the Jahn–Teller effect in CuO_6 coordination polyhedra. For this reason the hypothesis of the phase transition of malachite, $Cu_2CO_3(OH)_2$, to a rosasite structure at high pressure, as a result of the reduced Jahn–Teller effect, has been tested and confirmed by powder and single-crystal diffraction structural studies: above 6 GPa the malachite structure is no longer stable and transforms to a RS structure. RS $Cu_2CO_3(OH)_2$ is 3% more dense than malachite and the bulk modulus is remarkably higher, 80 (2) GPa compared with 48 (4) GPa. The longer apical Cu—O bonds in the distorted Me1 octahedral site are progressively shortened with increasing pressure, revealing a decrease in the Jahn–Teller effect at high pressure. The transition has a first-order character, is reversible with a significant hysteresis, and there is no evidence of any intermediate phase between the two structures. We then have further evidence that in the $Me_2(CO_3)(OH)_2$ compounds, the two main structural types, MS and RS, are closely related. The former structure is stabilized only when Cu is the prevalent cation in the octahedral sites, and it can transform directly to the RS as a function of thermodynamic changes.

1. Introduction

Malachite, $Cu_2CO_3(OH)_2$, is a common secondary copper mineral, belonging to the malachite–rosasite $(Cu,Zn)_2CO_3(OH)_2$ mineral group with the general formula $Me_2^{2+}CO_3(OH)_2$. Various phases can be found in this group (Table 1) and several mineralogical species are found in nature in complex thermodynamical systems such as meteorites and ore deposits. However, interest in these simple hydroxycarbonate salts arises as they are extensively employed in industrial processes. $(Cu,Zn)_2CO_3(OH)_2$ is in fact the primary phase involved in the production of Cu/ZnO-based catalysts, used in methanol synthesis, a chemical process with outstanding economic importance (Porta *et al.*, 1988; Bems *et al.*, 2003; Behrens *et al.*, 2009, 2010; Behrens & Girgsdies, 2010). $Ni_2CO_3(OH)_2$ and $Co_2CO_3(OH)_2$ are important phases recently employed in nanotechnology, and they can constitute

Table 1
Summary data for malachite and rosasite mineral groups, with the general formula $Me_2CO_3(OH)_2$.

Me1	Me2	Mineral name	Structure type	Space group	*a*	*b*	*c*	*β*	*V*	Ref.
Cu	Cu	Malachite	Malachite	$P2_1/a$	9.502	11.974	3.24	98.75	364.35	(*a*)
Cu	Zn	Rosasite	Rosasite	$P2_1/a$	12.8976 (3)	9.3705 (1)	3.1623 (1)	110.262 (3)	358.54 (3)	(*b*)
Cu	Mg	Mcguinessite	Rosasite	$P2_1/a$	12.9181 (4)	9.3923 (2)	3.1622 (1)	111.233 (3)	357.63 (3)	(*b*)
Cu	Ni	Glaukosphaerite	Rosasite	$P2_1/a$	12.8821 (4)	9.3653 (4)	3.1361 (1)	112.032 (5)	350.73 (4)	(*c*)
Mg	Mg	Pokrovskite	Rosasite	$P2_1/a$	13.1279 (4)	9.3506 (4)	3.1578 (1)	112.113 (5)	359.12 (4)	(*c*)
Fe	Fe	Chukanovite	Rosasite	$P2_1/a$	13.1693 (9)	9.407 (1)	3.2152 (3)	111.153 (6)	371.47 (5)	(*d*)
Cu	Co	Kolwezite	Rosasite	$P2_1/a$	12.8522 (9)	9.3584 (8)	3.1498 (5)	109.911 (6)	356.2 (6)	(*c*)
Ni	Ni	Nullaginite	Nullaginite	$P2_1/m$	9.236 (3)	12.001 (6)	3.091 (2)	90.48 (7)	342.6 (2)	(*e*)

References: (*a*) Zigan *et al.* (1977); (*b*) Perchiazzi (2006); (*c*) Perchiazzi & Merlino (2006); (*d*) Pekov *et al.* (2007); (*e*) Nickel & Berry (1981).

either the final nanomaterial (Yang *et al.*, 2011) or they are transient phases within the nanopreparation process (Zhu *et al.*, 2011). $Fe_2CO_3(OH)_2$ is a relatively common alteration product found in industrial plants (Ruhl *et al.*, 2011) or in natural altered Fe-bearing systems (Pekov *et al.*, 2007; Saheb *et al.*, 2011).

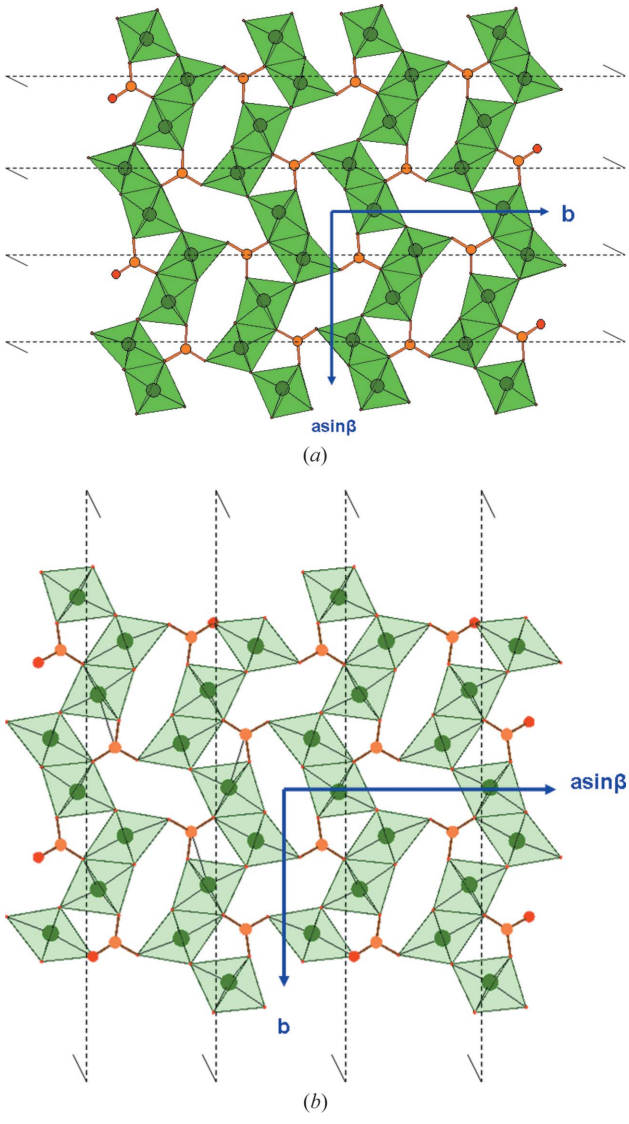

Figure 1
Comparison of the crystal structures of malachite (upper image) and rosasite (lower image), as seen along the *c* direction. It is worth noticing the different orientation of the symmetry elements with respect to the topology of malachite and rosasite.

The crystal structures proposed between 1960 and 1990 indicated substantial structural complexity in the general $Me_2^{2+}CO_3(OH)_2$ system. However, more recent advances in the accuracy of crystallographic analysis showed that these phases crystallize mainly within only two structural types, the malachite structure (MS) and the rosasite structure (RS). Only the mineral nullaginite, $Ni_2(CO_3)(OH)_2$ (Nickel & Berry, 1981), is still missing a novel structure redetermination. Both malachite and rosasite structures can be described with the same modules, namely 'ribbons' of Me^{2+} octahedra, comprising edge-sharing double octahedral chains elongated along the *c* axis and interconnected through corner-sharing (Fig. 1) to form 'corrugated' octahedral layers. The connection between adjacent layers is assured by triangular carbonate CO_3 groups. The difference between MS and RS is apparent considering the resulting symmetry and three-dimensional structure from the repetition of these structural layers. In MS the layer stacking yields a twofold screw axis perpendicular to the slabs, constraining the resulting monoclinic cell geometry. In RS, by contrast, there is a twofold screw axis parallel to the layers. The symmetry is still monoclinic, but the cell and the monoclinic angle are differently oriented, and the unique monoclinic angle is in the plane parallel to the slabs in MS and perpendicular in RS. The resulting space group, $P2_1/a$, is the same in both structures, but with a different crystal axes orientation with respect to the structure. If we describe rosasite with the same orientation of lattice parameters as MS, the space group is $P2_1/b11$, which reveals an evident difference in crystal structure.

MS is observed only in Cu-rich compositions. For this reason it has been proposed that the Jahn–Teller octahedral coordination distortion of CuO_6 polyhedra plays a fundamental role in stabilizing the malachite structure. The Cu^{2+} cations in MS possess a strongly distorted octahedral coordination, with two longer apical bonds (2.55 Å in the Me1 site and 2.32 Å in the Me2 site) compared with the other four in plane bonds (1.90 Å in Me1 and 1.95 Å in Me2; Zigan *et al.*, 1977). Jahn–Teller distortion is particularly evident in the Me1 site. The chemical substitution of Cu with other cations with a more regular octahedral coordination promotes partial cation ordering in the two octahedral sites of the structure, also

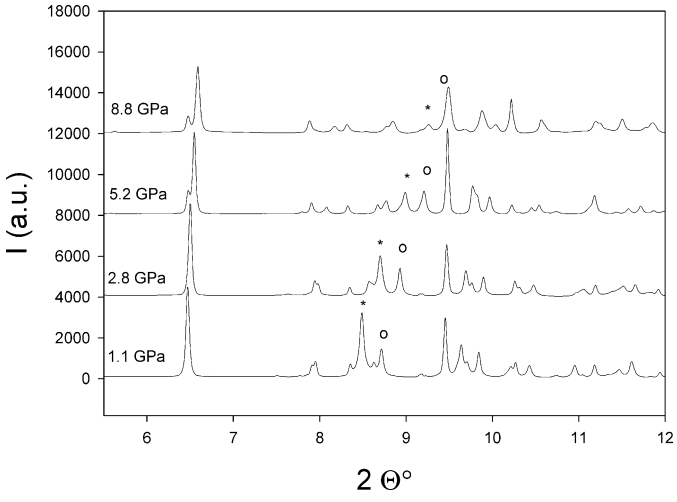

Figure 2
Selected X-ray powder pattern of malachite collected at high pressure ($\lambda = 0.414$ Å). Bragg peaks ($20\bar{1}$) and (211) in the angular region 8–9.5 are marked by an asterisk and circle, respectively. The relative change in intensity, in particular the remarkable decrease in intensity of the ($20\bar{1}$) peak and the increase of ($2\bar{1}1$) intensity, is apparent.

according to the slightly different site volumes. When these cations become dominant with respect to Cu in one octahedral Me site, the crystal structure shifts from MS to RS.

Attempts to synthesize solid solution terms in the Cu–Zn system with a close sampling failed, hindering a structural investigation close to the MS to RS transition, and discussion of the nature of the transition from one form to another is only speculative.

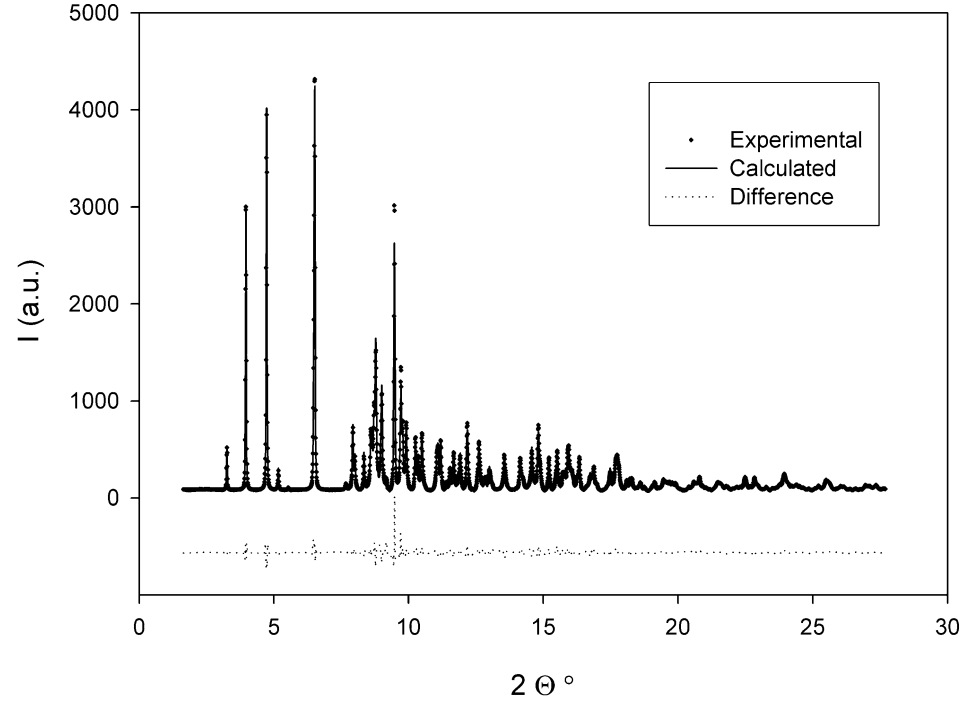

Figure 3
Rietveld fit of the experimental X-ray powder pattern of malachite collected at 3.4 GPa.

Since it is well known that high pressure can promote a reduction of the Jahn–Teller effect in transition metals, we performed a high-pressure structural investigation in pure malachite with the main aim of verifying whether, at high pressure, an expected decrease of the Jahn–Teller distortion would trigger a structural transition in malachite, and therefore investigate the structural details of a possible high-pressure transition.

2. Experimental

We performed structural investigations at high pressure at the ESRF synchrotron facility, ID09A beamline, with powder and single-crystal samples. A natural malachite sample was used. Microprobe analysis confirmed no other cations were present, within experimental accuracy, indicating a chemical formula of pure $Cu_2CO_3(OH)_2$. The high-pressure cell used was a membrane-type diamond–anvil cell (600 µm diameter culet, stainless steel gasket, gasket hole 250 µm in diameter). The standard experimental setup of the beamline was used (monochromatic parallel beam, $\lambda = 0.414$ Å, 30×20 µm^2 section on the sample, mar555 detector).

Powder data were processed with *Fit*2D and *GSAS* software (Hammersley *et al.*, 1996; Larson & Von Dreele, 1988). Single crystal data were handled with *CrysAlis* and *JANA*2006 software (Oxford diffraction, 2008; Petricek *et al.*, 2006), after preliminary raw data conversion and preparation with a code available at the beamline.

The powder experiments were performed using a mixture of methanol and ethanol as a pressure-transmitting medium. Pressure was determined by the ruby method (Mao *et al.*, 1986). Initial powder diffraction experiments surprisingly showed that the intense X-ray beam and methanol:ethanol mixture partially decomposed malachite, forming metallic Cu after long X-ray beam exposure (*i.e.* 60 s, the average time used for sample alignment). Short exposures, on the contrary, did not promote any sample decomposition. We then performed the experiment aligning the sample only by optical methods and performing data collection with an exposure time of 0.25 s with the maximum beam intensity available. With this strategy a single sample survived for the duration of the experiment.

The single-crystal experiment was performed with He as the pressure-transmitting medium. The single crystal used had the approximate dimensions $40 \times 10 \times 10$ µm. Pressure was measured using the ruby scale.

3. Results and discussion

3.1. X-ray powder diffraction

Selected integrated powder patterns representative of the behavior of malachite at high pressure are reported in Fig. 2. A strong preferred orientation, mainly due to the [001] acicular crystal habit, was modeled with refinement of spherical harmonic coefficients to sixth order. A fit of the experimental data with the MS model is satisfactory up to 7 GPa (Fig. 3 and Table 2). Above 7 GPa the fit of the data with the MS model yields distinctly higher agreement factors and new peaks are not indexed. The evolution of powder patterns with pressure reveals the same features observed in powder patterns within the malachite–rosasite series, namely the progressive shift of the diffractions $(\bar{2}01)$ and $(21\bar{1})$ to higher angles, in a more pronounced way than the other peaks due to simple compression. The shift in angle for these diffractions is known in natural malachites when Cu is progressively substituted by other cations with more regular octahedral coordination (Porta *et al.*, 1988; Deliens *et al.*, 1973; Jambor, 1976). The structural interpretation of this feature is recent (Behrens & Girgsdies, 2010) and correlates the shift in 2θ of the above-mentioned peaks, and the simultaneous strong contraction of the *a* and *c* cell parameters, with the shrinkage of the apical bonds of the Cu octahedra. There is also a significant decrease of intensity at higher pressure for the $(\bar{2}01)$ peak and a relative increase in intensity for the $(21\bar{1})$ peak, as would be expected in an MS to RS structure transition (Perchiazzi, 2006). An attempt to perform a fit with the RS model did not reduce agreement factors, and few peaks of malachite, in particular the $(\bar{2}01)$, remained unfitted. An excellent fit of the data above 7 GPa on the contrary was achieved if both MS and RS models are used to define a mixed-phase model (Figs. 4 and 5). Phase proportion estimation by the Rietveld method indicated a progressive reduction of MS and a consequent increase of RS content as a function of pressure (RS from 32% at 7.5 GPa, to 45% at 8.8 GPa and finally 88% at 9.8 GPa).

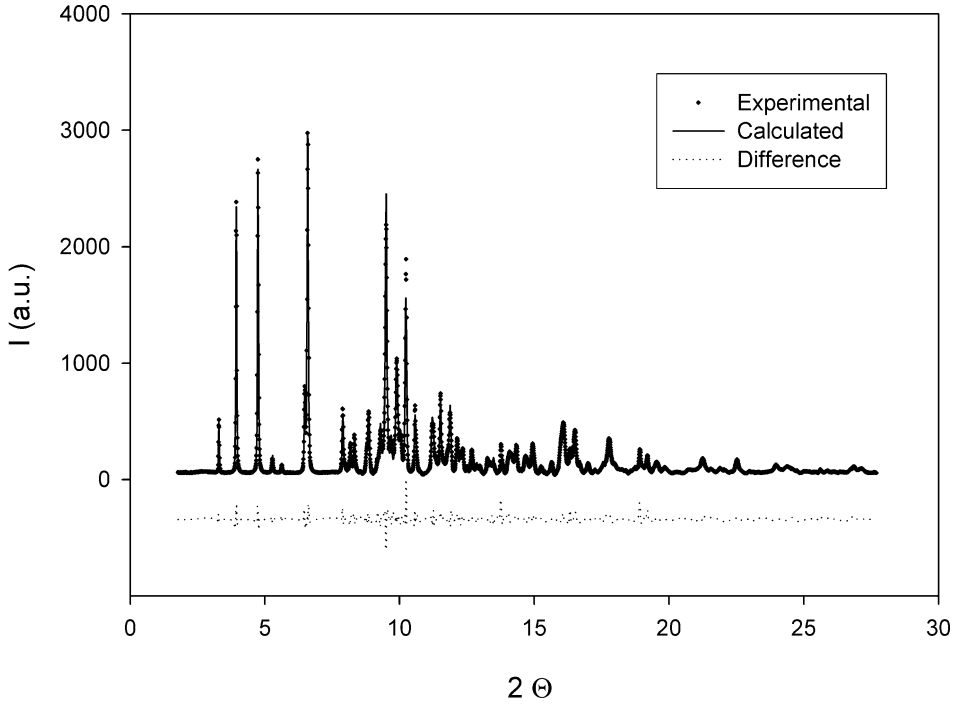

Figure 4
Rietveld fit of the experimental X-ray powder pattern of $Cu_2CO_3(OH)_2$ collected at 8.8 GPa, performed with RS and MS structural types.

3.2. Single-crystal diffraction

The MS to RS structure transition is confirmed by single-crystal diffraction performed in the 0–10 GPa pressure range. An attempt to select an untwinned crystal failed, and a crystal twinned, as is usual for malachite, with (100) as the twinning plane was used. Twinning was incorporated into the crystal structure refinement models, with datasets integrated on the two individuals. The refined twin fractions vary slightly in the different refinements, probably because of the crystal orientation with respect to the beam, with an average close to 0.5. Preliminary refinements showed a variable C—O distance with a significant scatter of the data, however, clustering around an average value of 1.29 Å. In order to extract more accurate values we therefore constrained C—O distances, taking into account the C—O distance variation with pressure in carbonates (Ross & Reeder, 1992) combined with recent data collected at the ID09 beamline on a siderite single crystal: the C–O distance varies approximately linearly within the pressure range 0–10 GPa and the fitted line: d(Å) = 1.2925–9.372E-4*P (GPa) was used to constrain C—O distances at the various experimental pressures.

Above 6 GPa diffraction peaks could only be indexed with a different monoclinic cell. Cell parameter values are similar, but the main difference compared with the original malachite cell is the monoclinic angle, which is α rather than β, which is characteristic of a transformation to a RS structure. The integrations were performed with this new cell and transformed into the standard setting (*b* unique) for the RS space-group symmetry. Crystal structure refinements were performed with the starting atomic coordinates of rosasite (Perchiazzi, 2006). Rosasite is also twinned, with (100) as the twinning plane. Figs. 6 and 7 report the equatorial reciprocal lattice planes perpendicular to the cell axis with a periodicity of $\sim$ 12 Å, recorded at 4.1 and 7.2 GPa. It is worth noticing that this periodicity corresponds to the twofold symmetry axis in the MS (*b* in standard setting) and the *a* axis in the *RS* structure. It can be seen that at lower pressure (Fig. 6)

Table 2
Results of powder diffraction experiments.

P (GPa)	Malachite (wt %)	Rosasite (wt %)	wR_p	rF^2	*a*	*B*	*c*	*B*	Volume	Note
0.51	100	0	0.132	0.075	9.445 (4)	11.950 (3)	3.217 (1)	98.26 (3)	359.33 (8)	
1.16	100	0	0.108	0.078	9.401 (3)	11.951 (2)	3.195 (1)	97.82 (2)	355.59 (7)	
1.57	100	0	0.108	0.113	9.371 (3)	11.953 (2)	3.181 (1)	97.52 (2)	353.19 (7)	
2.09	100	0	0.109	0.107	9.336 (3)	11.958 (2)	3.161 (1)	97.16 (2)	350.20 (7)	
2.83	100	0	0.133	0.104	9.285 (3)	11.97 (2)	3.134 (1)	96.63 (2)	346.03 (7)	
3.4	100	0	0.082	0.045	9.242 (3)	11.981 (2)	3.114 (1)	96.23 (2)	342.72 (7)	
4.5	100	0	0.114	0.081	9.172 (3)	12.007 (2)	3.079 (1)	95.5 (2)	337.49 (7)	
5.18	100	0	0.111	0.068	9.137 (3)	12.022 (2)	3.06 (1)	95.14 (2)	334.78 (7)	
6.16	100	0	0.121	0.155	9.098 (3)	12.045 (2)	3.033 (1)	94.63 (2)	331.33 (7)	
7.56	100	0	0.149	0.107	9.040 (5)	12.049 (4)	3.003 (2)	94.04 (4)	326.31 (9)	
	0	100	0.229	0.241	12.603 (9)	9.020 (7)	2.982 (3)	106.98 (9)	324.3 (4)	
	68.5 (5)	31.5 (9)	0.089	0.056	9.040 (5)	12.049 (2)	3.003 (1)	94.04 (4)	326.31 (7)	Malachite
					12.601 (9)	9.030 (4)	2.986 (3)	107.04 (8)	324.8 (2)	Rosasite
8.83	100	0	0.197	0.209	9.024 (5)	12.046 (4)	2.994 (2)	93.93 (4)	324.69 (9)	
	0	100	0.173	0.167	12.601 (9)	9.005 (7)	2.975 (3)	106.99 (9)	322.80 (4)	
	52.8 (5)	47.2 (9)	0.095	0.096	9.011 (5)	12.043 (2)	2.994 (1)	93.80 (4)	324.16 (7)	Malachite
					12.603 (9)	9.015 (4)	2.976 (3)	107.07 (8)	323.27 (2)	Rosasite
9.78	100	0	0.217	0.299	9.019 (5)	12.032 (7)	2.989 (5)	93.93 (9)	323.6 (9)	
	0	100	0.203	0.138	12.591 (9)	8.998 (7)	2.972 (3)	107.02 (4)	321.92 (4)	
	11.9 (9)	88.1 (5)	0.103	0.152	9.004 (5)	12.049 (5)	2.986 (3)	93.65 (8)	323.31 (7)	Malachite
					12.582 (9)	9.004 (4)	2.976 (3)	107.05 (4)	322.27 (7)	Rosasite

the angle between reciprocal lattice vectors is β^*. In the higher-pressure pattern (Fig. 7) this angle is 90°, the monoclinic angle being the one between the ∼9 Å and the ∼3 Å axes in the RS setting. Systematic extinctions are in agreement with the different cell setting, as clearly visible in both the figures. In the *h*0*l* plane of malachite (Fig. 6) the diffractions $h = 2n + 1$ are extinct due to the presence of the *a* glide plane. On the other hand the 0*kl* plane of rosasite, according to the *RS* setting, as reported in Fig. 7, shows only the screw extinction condition $k = 2n + 1$. The diffraction peaks are sharp after the phase transition and there is no evidence of an increased mosaicity at high pressure. The results of single-crystal refinements are summarized in Tables 3 and 4, and the structural features are described in the following paragraphs.

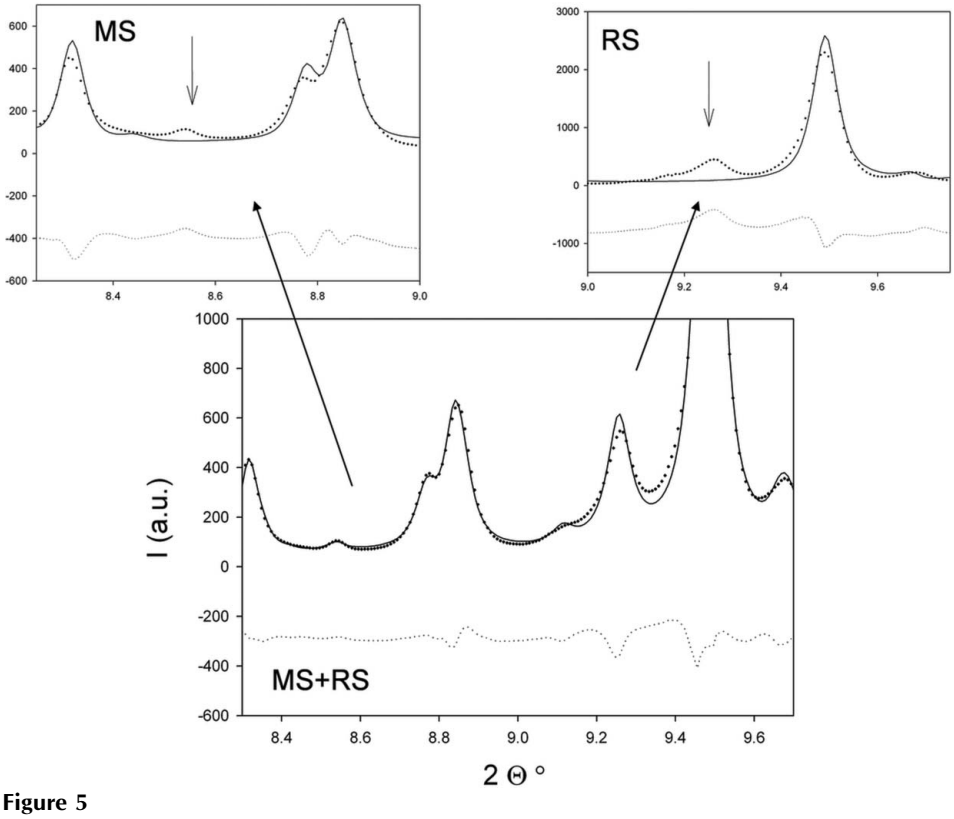

Figure 5
Enlarged view of the fit reported in Fig. 4 relative to the Rietveld fit performed using both MS and RS models of the powder pattern collected at 8.8 GPa, in the angular range 8–10 ° (bottom) and zoomed view of two portions of the pattern fitted with MS only (top left) and RS only (top right) structure. It is apparent that the best fit of all the diffraction peaks is achieved only supposing that both phases are present.

3.3. High-pressure behaviour of the MS phase

Lattice parameters of malachite at the various pressures are reported in Tables 2 and 3. Malachite shrinks along the *a* and *c* directions, while on the contrary *b* shows a slight expansion. This is in agreement with a proposed structural explanation (Porta *et al.*, 1988). Nevertheless, if we extrapolate the trend of the β monoclinic angle of the single-crystal data, we can infer that β is ∼94.5° at the structural transition from MS to RS. A value significantly larger than 90° is also suggested by the mixed-phase Rietveld refinement of powder data at increasing pres-

Table 3
Summary of single-crystal data analysis.

Lattice parameters and the refinement statistical factor (obs = observed: $I > 3\sigma$; all = all reflections) are reported. The last two points (*a* rosasite, *b* malachite) have been collected during decompression, and only lattice parameters were determined.

P (Gpa)	*a*	*b*	*c*	β	*V*	No. refl.	R_{obs}	R_{all}	GoF all	GoF obs	Twin fraction
0.02 (5)	9.473 (2)	11.977 (7)	3.2377 (5)	98.71 (2)	363.13 (4)	455	0.0897	0.130	6.77	5.63	0.36 (5)
1.02 (5)	9.389 (2)	11.968 (7)	3.1960 (5)	97.93 (2)	355.67 (4)	423	−0.0748	0.086	4.94	4.59	0.52 (5)
2.03 (5)	9.317 (2)	11.977 (7)	3.1597 (5)	97.18 (2)	349.86 (4)	704	0.0641	0.067	3.67	3.29	0.33 (5)
3.1 (5)	9.236 (2)	11.987 (7)	3.1205 (5)	96.17 (2)	343.38 (4)	546	0.0667	0.0705	4.12	3.73	0.38 (5)
4.06 (5)	9.183 (2)	12.023 (7)	3.0886 (5)	95.73 (2)	339.15 (4)	605	0.0737	0.09	5.11	4.35	0.38 (5)
5.17 (5)	9.114 (2)	12.053 (7)	3.0574 (5)	95.03 (2)	334.64 (4)	612	0.0824	0.128	5.43	4.87	0.5 (5)
6.22 (5)	12.699 (7)	9.039 (2)	2.9943 (5)	107.18 (2)	328.39 (4)	664	0.125	0.166	9.23	7.67	0.55 (5)
7.14 (5)	12.667 (7)	9.015 (2)	2.9827 (5)	107.13 (2)	325.49 (4)	622	0.0913	0.159	5.00	4.4	0.54 (5)
8.29 (5)	12.624 (7)	8.993 (2)	2.9704 (5)	107.08 (2)	322.29 (4)	594	0.0671	0.084	5.05	4.5	0.53 (5)
9.58 (5)	12.582 (7)	8.965 (2)	2.9572 (5)	107.05 (2)	318.92 (4)	630	0.0984	0.126	7.17	6.13	0.57 (5)
4.63 (5)[a]	12.774 (7)	9.088 (2)	3.0133 (5)	107.25 (2)	334.05 (4)						
3.19 (5)[b]	9.229 (2)	12.006 (7)	3.1155 (5)	96.35 (2)	343.10 (4)						

sures. Our data hence do not support the necessity of an orthorhombic phase as an intermediate structure (Behrens & Girgsdies, 2010), since MS and RS can transform directly into each other. Fig. 8 shows the volume variation with increasing pressure. In this figure both powder and single-crystal data are reported for MS, whereas for clarity only the more accurate single-crystal data have been plotted for the RS phase. In fact, the presence of two phases in the high-pressure powder data ($P > 7$ GPa) could introduce strong correlations during refinements of lattice parameters of the two phases, which are actually very similar. Both single-crystal and powder data (Tables 2 and 3) indicate that the RS phase is more dense than malachite. A fit of the malachite volume data with a third-order Birch–Murnagham equation of state (EoS) give comparable results both on powder and single-crystal experimental volume data: $K_0 = 48$ (4) GPa, $K' = 7.0$ (16) and $V_0 = 363.5$ (7) Å^3 (powder data) and $K_0 = 43$ (3), $K' = 9.2$ (16) and $V_0 = 363.4$ (4) Å^3 (single-crystal data). The high K' value highlights some features in the evolution of the structure, and it is likely correlated to the evolution of CuO_6 coordination polyhedra, as a consequence of electronic change with increasing pressure. The results of structural refinements (atomic coordinates and selected bond distances) are summarized in Table 4. The variation of apical and equatorial chemical bonds (Fig. 9) confirms the remarks made about lattice parameter variations. Regularization of the coordination octahedral site is also expressed by variation of the Δ parameter (Eby & Hawthorne, 1993), defined as

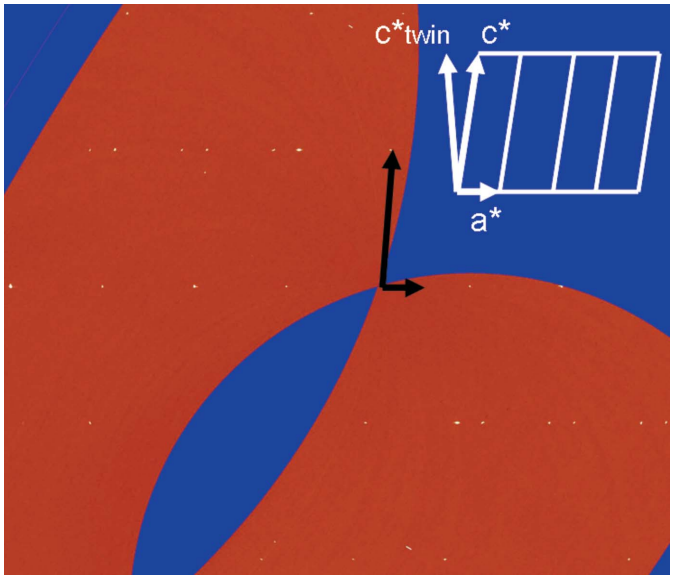

Figure 6
*h*0*l* reciprocal plane reconstruction of malachite. The data have been collected at 4.1 GPa. The *a** and *c** reciprocal axes are displayed in the figure and a schematic portion of the lattice is also represented, together with the orientation of the twin *c** axis. Systematic extinction is compatible with the $P2_1/a$ cell setting: $h = 2n$ in the *h*0*l* plane

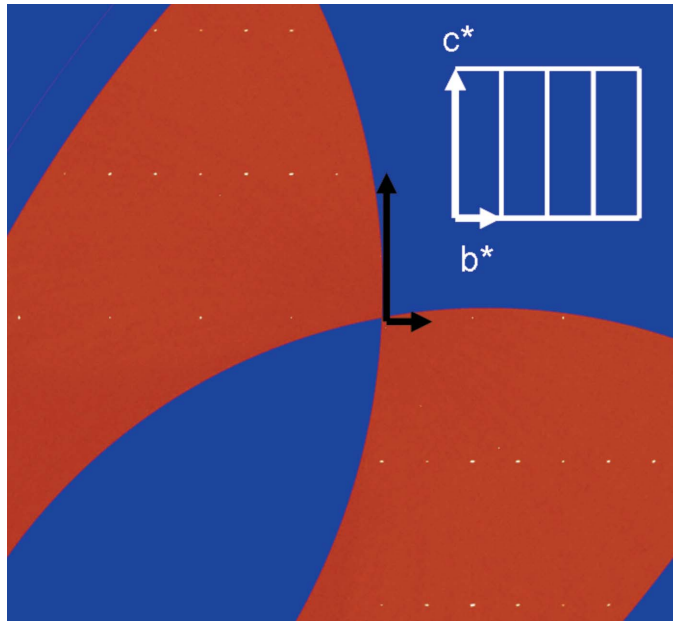

Figure 7
0*kl* reciprocal plane reconstruction in the rosasite cell setting (corresponding to the *h*0*l* orientation of malachite) performed with data collected at 7.1 GPa. The angle between the two axes is 90° and the systematic extinctions are in agreement with the space group $P2_1/a$: $k = 2n$ in the 0*k*0 direction, and no condition in the general 0*kl* plane.

Table 4
Single-crystal refinement results.

Atomic coordinates, selected bond distances and Δ distortion parameters are reported. The errors are of the order 0.0001–0.001 Å for atomic coordinates, 0.005–0.02 Å for interatomic distances and 0.0002 for Δ parameters.

	MS structure				RS structure					
P	0.02 GPa	1.02 GPa	2.03 GPa	3.1 GPa	4.06 GPa	5.17 GPa	6.22 GPa	7.14 GPa	8.29 GPa	9.58 GPa
Cu1 *x*	0.4998 (5)	0.4998 (3)	0.5008 (2)	0.5022 (2)	0.5033 (3)	0.5044 (2)	0.2063 (9)	0.2101 (5)	0.2093 (4)	0.2081 (6)
y	0.2882 (9)	0.2882 (6)	0.2886 (4)	0.2888 (5)	0.2888 (5)	0.2888 (5)	0.0101 (5)	0.0108 (3)	0.0119 (2)	0.0130 (4)
z	0.8936 (12)	0.8874 (8)	0.8808 (6)	0.8745 (9)	0.8717 (8)	0.8638 (9)	0.439 (2)	0.4450 (12)	0.4408 (10)	0.4362 (15)
U_{iso}	0.0113 (15)	0.0107 (11)	0.0139 (7)	0.0149 (10)	0.0134 (9)	0.0138 (9)	0.0127 (17)	0.0134 (10)	0.022 (3)	0.0125 (13)
Cu2 *x*	0.2324 (4)	0.2327 (3)	0.2329 (2)	0.2331 (2)	0.2328 (3)	0.2341 (3)	0.3910 (5)	0.3927 (5)	0.3932 (4)	0.3924 (7)
y	0.3929 (9)	0.3934 (6)	0.3936 (4)	0.3937 (4)	0.3941 (5)	0.3942 (5)	0.2361 (2)	0.2371 (2)	0.2381 (2)	0.2390 (4)
z	0.3888 (10)	0.3851 (7)	0.3805 (5)	0.3755 (7)	0.3700 (7)	0.3670 (7)	0.1815 (10)	0.1859 (10)	0.1883 (9)	0.1892 (14)
U_{iso}	0.0086 (15)	0.0098 (11)	0.0127 (7)	0.0131 (9)	0.0138 (9)	0.0127 (9)	0.0136 (17)	.0101 (10)	0.022 (2)	0.0131 (13)
O1 *x*	0.132 (2)	0.1311 (13)	0.131 (10)	0.1345 (11)	0.1336 (14)	0.1351 (11)	0.128 (4)	0.132 (2)	0.131 (2)	0.129 (3)
y	0.137 (5)	0.135 (3)	0.136 (2)	0.139 (2)	0.137 (3)	0.136 (2)	0.141 (2)	0.144 (11)	0.1432 (10)	0.146 (15)
z	0.343 (7)	0.337 (4)	0.334 (3)	0.325 (4)	0.321 (5)	0.315 (4)	0.775 (11)	0.791 (6)	0.768 (5)	0.761 (8)
U_{iso}	0.024 (7)	0.011 (4)	0.022 (3)	0.019 (4)	0.028 (5)	0.008 (4)	0.017 (8)	0.009 (4)	0.014 (3)	0.01 (6)
O2 *x*	0.342 (2)	0.3399 (16)	0.3377 (10)	0.3407 (12)	0.3406 (13)	0.3448 (13)	0.231 (3)	0.2308 (18)	0.2319 (15)	0.231 (2)
y	0.235 (3)	0.237 (2)	0.233 (13)	0.2255 (15)	0.2341 (18)	0.2298 (17)	0.355 (2)	0.3559 (13)	0.3540 (11)	0.3571 (16)
z	0.459 (7)	0.448 (5)	0.437 (3)	0.430 (4)	0.427 (4)	0.409 (5)	0.884 (9)	0.883 (5)	0.892 (4)	0.902 (7)
U_{iso}	0.016 (7)	0.015 (4)	0.009 (3)	0.018 (4)	0.016 (4)	0.019 (4)	0.003 (7)	0.013 (4)	0.012 (4)	0.004 (5)
O3 *x*	0.335 (2)	0.3386 (14)	0.337 (10)	0.339 (12)	0.3401 (13)	0.3434 (11)	0.055 (3)	0.06 (2)	0.0611 (16)	0.057 (2)
y	0.059 (3)	0.054 (2)	0.0524 (13)	0.0572 (16)	0.0536 (18)	0.0582 (17)	0.342 (2)	0.3478 (13)	0.350 (11)	0.3495 (18)
z	0.633 (6)	0.635 (4)	0.6276 (3)	0.630 (4)	0.624 (4)	0.630 (4)	0.400 (8)	0.398 (5)	0.414 (4)	0.409 (6)
U_{iso}	0.012 (6)	0.006 (4)	0.011 (3)	0.012 (4)	0.014 (4)	0.002 (3)	0.00 (7)	0.017 (5)	0.012 (3)	0.01 (5)
O4 *x*	0.083 (2)	0.094 (15)	0.091 (10)	0.0941 (11)	0.0935 (14)	0.0965 (12)	0.360 (5)	0.357 (2)	0.352 (3)	0.358 (4)
y	0.347 (5)	0.346 (3)	0.353 (2)	0.348 (2)	0.348 (3)	0.349 (2)	0.103 (2)	0.1048 (11)	0.106 (12)	0.1057 (16)
z	0.918 (6)	0.906 (4)	0.905 (3)	0.892 (4)	0.880 (5)	0.876 (4)	0.656 (10)	0.641 (5)	0.642 (5)	0.665 (7)
U_{iso}	0.009 (6)	0.012 (4)	0.015 (3)	0.01 (4)	0.02 (4)	0.009 (4)	0.008 (7)	−0.001 (4)	0.022 (4)	0.006 (5)
O5 *x*	0.3779 (17)	0.3797 (13)	0.382 (9)	0.3817 (11)	0.3778 (12)	0.382 (12)	0.430 (4)	0.427 (2)	0.428 (2)	0.429 (3)
y	0.409 (4)	0.418 (3)	0.4193 (19)	0.416 (2)	0.417 (2)	0.417 (3)	0.384 (2)	0.3832 (12)	0.3859 (12)	0.3875 (18)
z	0.860 (4)	0.858 (3)	0.849 (2)	0.847 (4)	0.846 (4)	0.850 (4)	−0.256 (10)	−0.267 (6)	−0.266 (5)	−0.262 (8)
U_{iso}	0.00 (5)	0.002 (4)	0.011 (3)	0.013 (4)	0.012 (4)	0.015 (4)	0.016 (7)	0.011 (4)	0.019 (3)	0.017 (6)
C *x*	0.268 (2)	0.273 (13)	0.2663 (10)	0.2677 (12)	0.2706 (14)	0.2703 (12)	0.152 (3)	0.1459 (18)	0.1351 (15)	0.14 (2)
y	0.145 (3)	0.146 (2)	0.1485 (13)	0.1501 (16)	0.138 (18)	0.1377 (17)	0.286 (2)	0.2837 (12)	0.2868 (11)	0.2869 (16)
z	0.461 (10)	0.461 (6)	0.456 (5)	0.455 (6)	0.444 (6)	0.440 (6)	0.737 (11)	0.780 (7)	0.699 (6)	0.712 (9)
U_{iso}	0.010 (10)	0.001 (6)	0.016 (5)	0.007 (6)	0.016 (6)	0.006 (5)	0.008 (10)	0.017 (7)	0.029 (6)	0.012 (8)
Cu1—O	2.118 (9)	2.129 (9)	2.130 (9)	2.105 (9)	2.096 (9)	2.077 (9)	2.139 (9)	2.105 (9)	2.091 (9)	2.101 (9)
Cu2—O	2.156 (9)	2.129 (9)	2.112 (9)	2.099 (9)	2.084 (9)	2.089 (9)	2.072 (9)	2.082 (9)	2.065 (9)	2.056 (9)
Δ Cu1	0.0221 (2)	0.0174 (2)	0.0146 (2)	0.0136 (2)	0.0127 (2)	0.0113 (2)	0.0056 (2)	0.0057 (2)	0.0066 (2)	0.0054 (2)
Δ Cu2	0.0079 (2)	0.0058 (2)	0.0058 (2)	0.0041 (2)	0.0034 (2)	0.0028 (2)	0.0023 (2)	0.0033 (2)	0.0022 (2)	0.0025 (2)
O1—O5	2.721 (5)	2.714 (5)	2.696 (5)	2.691 (5)	2.707 (5)	2.692 (5)	2.622 (7)	2.540 (8)	2.549 (7)	2.516 (8)
O3—O4	2.642 (5)	2.690 (5)	2.664 (5)	2.664 (5)	2.663 (5)	2.692 (5)	2.641 (7)	2.552 (8)	2.589 (7)	2.570 (8)

$$\Delta = \frac{1}{6}\Sigma\left[\frac{(l_i - l_0)}{l_0}\right]^2 \quad (1)$$

and reported in Fig. 10. It is also apparent that the Me1 octahedra, *i.e.* that presenting the stronger Jahn–Teller distortion, becomes more regular with increasing pressure. Hydrogen bonds are important in the malachite structure, especially for the charge balance of O1 and O3, which are bonded to C and to one octahedral Me^{2+} only. They also strengthen the structure, assuring further connections between the octahedral framework and the carbonate groups. In Table 4 the O:::O bond distances are reported at the various pressures. The longer O1:::O5 bond shrinks from 2.8 Å at ambient pressure to 2.68 Å at higher pressure (5.17 GPa), while the shorter O4:::O3 bond length remains approximately around 2.65 Å at higher pressure.

3.4. HP behaviour of the RS phase

Above 6–7 GPa both powder and single-crystal refinements indicate a transition towards an RS structure. The crystal structure refinement on single-crystal data confirmed that above 6 GPa malachite adopts the RS model. The compressibility of rosasite has been calculated using the volume derived by single-crystal data only, because the powder data were from a mixture of MS and RS phases with significant correlation in extracted parameters. The bulk modulus of the

high-pressure RS phase is 80 (2) GPa and V_0 is 351.6 (7) Å^3 (due to the scarce number of points and the lack of volume data at room pressure we used a Birch–Murnagham EoS with constrained $K = 4$). The RS phase is slightly more dense, and the extrapolation of volume data at room pressure indicates a 3.1% increase in density. The transition is reversible but with an evident hysteresis. These features and also the presence of two phases in the high-pressure powder data suggest the transition is first order. The possible presence of a high density of defects with associated remarkably high elastic energy in the single-crystal sample, and the energetic difficulty in changing the external crystal shape could trigger an almost instantaneous transition. Alternatively, the powder sample could have been annealed during the grinding procedure. For this reason, the MS to RS transition is likely driven by the nucleation and growth process, but the limited time available for pressure equilibration during powder experiments (about 20 min every pressure increase step) prevented attainment of thermodynamic equilibrium. Consistent with this kinetic explanation, the total amount of RS phase estimated by the Rietveld method markedly increases (Table 2) at each pressure step.

Tables 3 and 4 also report lattice parameters and atomic coordinates for the RS phase. The variation of lattice parameters is small in the *b* and *a* directions, and *c* presents the largest variation. This situation can be explained by the fact that the apical distances of Me1 octahedra are aligned along **b**. In MS the Cu1—O2 bond shrinks more than the shorter Cu1—O1 bond, but in rosasite no such anisotropy is observed. Bond distances and the distortion Δ parameter for the RS phase are also included in Figs. 9 and 10. It is noticeable that the Δ values are remarkably lower when compared with those of malachite within the 0–6 GPa range. Cu—O bond lengths shrink as a function of pressure even though it is much less compared with those of malachite, because the RS form of malachite is substantially more dense. The O:::O bond variations are less evident since they are already short, falling in the range 2.5–2.6 Å and so are significantly shorter than in the MS structure.

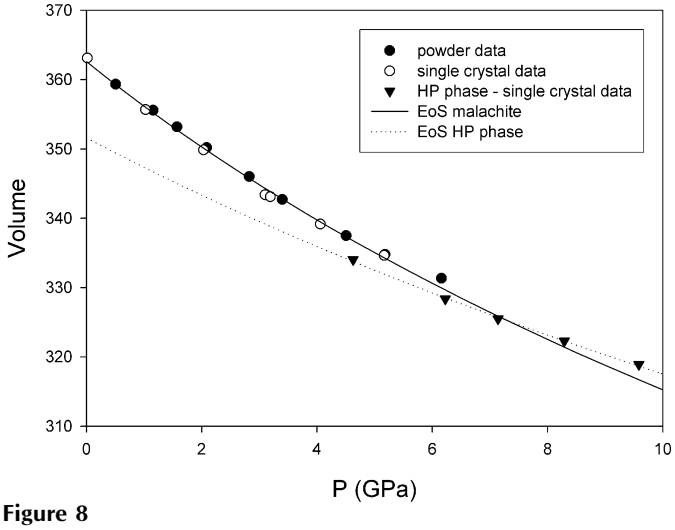

Figure 8
Volume variation of malachite as a function of pressure. The powder (filled circles) and single-crystal (empty circles) data are reported for malachite, together with the volume data for the high-pressure RS structure. The EOS for the MS and RS phases are also reported. The extrapolation of volume at ambient pressure for the HP phase indicates an increase of 3.1% in density (ρ_0 = 4.051 g cm^{-3} for MS and ρ_0 = 4.177 g cm^{-3} for the RS structure).

4. Conclusions

The elastic behaviour of malachite has been investigated and crystal structure determinations at high pressure have been performed on powder and single-crystal data. Above 6 GPa a phase transition from the MS to the RS is observed, this transition being related to a reduction of the Jahn–Teller effect at high pressure. The regularization of the Me2 site promotes a

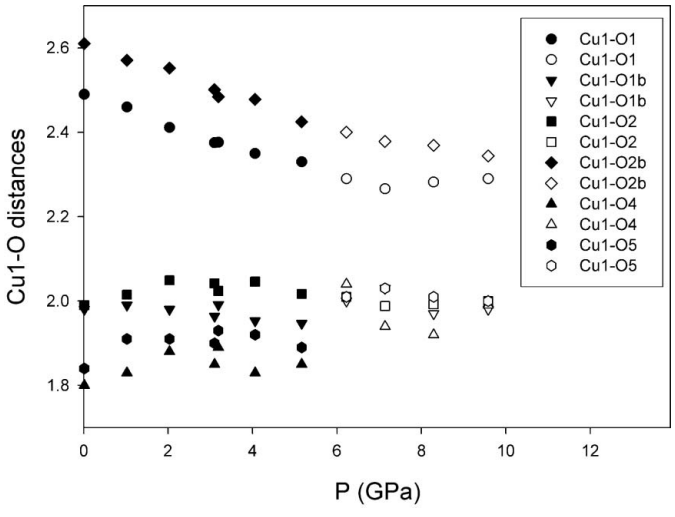

Figure 9
Cu—O bond distance in Me1 coordination polyhedra, the site presenting the highest Jahn–Teller distortion effect, as a function of pressure.

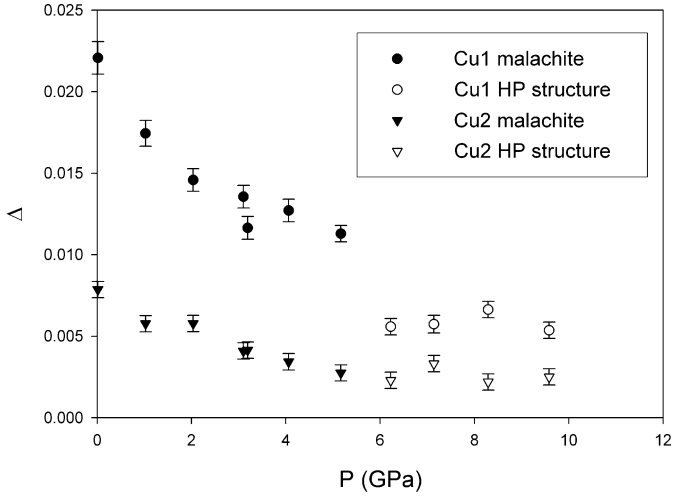

Figure 10
Variation of the Δ parameter as a function of pressure. Filled symbols: MS; empty symbols: RS structure; circles: Cu1 polyhedra; triangles: Cu2 polyhedra.

twist from the MS towards the RS structure. At ambient conditions the same transition towards the RS model is observed as a function of chemical substitution of Cu with cations requiring regular octahedral coordination, such as Zn (rosasite), Ni (glaukosphaerite), Co (kolwezite) and Mg (mcguinnessite). In all these phases, because of the reduction of the Jahn–Teller effect, the *RS* arrangement is realised. The phase transition (likely with a first-order character) from MS to RS proceeds directly without a transient phase between the two structures.

ESRF is acknowledged for provision of beamtime within the in-house research projects of ID09A beamline, and for supporting the visiting scientist activity of MM.

References

Behrens, M. & Girgsdies, F. (2010). *Z. Anorg. Allg. Chem.* **636**, 919–927.

Behrens, M., Girgsdies, F., Trunschke, A. & Schlogl, R. (2009). *Eur. J. Inorg. Chem.* **10**, 1347–1357.

Behrens, M., Kasatkin, I., Kuhl, S. & Weinberg, G. (2010). *Chem. Mater.* **22**, 386–397.

Bems, B., Schur, M., Dassenoy, A., Junkes, H., Herein, D. & Schlögl, R. (2003). *Chem. Eur. J.* **9**, 2039–2052.

Deliens, M., Oosterbosch, R. & Verbeck, T. (1973). *Bull. Soc. Fr. Miner. Crist.* **96**, 371–377.

Eby, R. K. & Hawthorne, F. C. (1993). *Acta Cryst.* B**49**, 28–56.

Hammersley, A. P., Svensson, S. O., Hanfland, M., Fitch, A. N. & Häusermann, D. (1996). *High Press. Res.* **14**, 235–248.

Jambor, J. L. (1976). Report of Activities, Part C. Geological Survey of Canada, Paper 76-1C, 97.

Larson, A. C. & Von Dreele, R. B. (1988). Report LAUR 86–748. Los Alamos National Laboratory, Los Alamos, New Mexico, USA.

Mao, H. K., Xu, J. & Bell, P. M. (1986). *J. Geophys. Res.* **91**, 4673–4776.

Nickel, E. H. & Berry, L. G. (1981). *Can. Mineral.* **19**, 315–324.

Oxford Diffraction (2008). *CrysAlis RED*, Version 1.171.32.29. Oxford Diffraction, Abingdon, England.

Pekov, I. V., Perchiazzi, N., Merlino, S., Kalachev, V. N., Merlini, M. & Zadov, A. (2007). *Eur. J. Mineral.* **19**, 891–898.

Perchiazzi, N. (2006). *Z. Kristallogr.* **23**, 505–510.

Perchiazzi, N. & Merlino, S. (2006). *Eur. J. Mineral.* **18**, 787–792.

Petricek, V., Dusek, M. & Palatinus, L. (2006). *JANA*2006. Institute of Physics, Praha, Czech Republic.

Porta, P., De Rossi, S., Ferraris, G., Lo Jacono, M., Minelli, G. & Moretti, G. (1988). *J. Catal.* **109**, 367–377.

Ross, N. L. & Reeder, R. J. (1992). *Am. Mineral.* **77**, 412–421.

Ruhl, A. S., Kotre, C., Genert, U. & Jekel, M. (2011). *Chem. Eng. J.* **172**, 811–816.

Saheb, M., Neff, D., Bellot-Gurlet, L. & Dillmann, P. (2011). *J. Raman Spectrosc.* **42**, 1100–1108.

Yang, J. J., Cheng, H. & Frost, R. L. (2011). *Spectrochim. Acta A*, **78**, 420–428.

Zhu, J. H., Jiang, J. A., Liu, J. P., Ding, R. M., Ding, H., Feng, Y. M., Wie, G. M. & Huang, H. T. (2011). *J. Solid State Chem.* **184**, 578–583.

Zigan, F., Joswig, W., Schuster, H. D. & Mason, S. A. (1977). *Z. Kristallogr.* **145**, 412–426.